(revised version of the paper Manuscript ID: TC-ART-04-2022-001680 to be submitted to Journal of Materials Chemistry C, June 2022)

Induced internal stresses and their relation to FLASH sintering of KNN ceramics

Ricardo Serrazina[1], Mariana Gomes[2], Rui Vilarinho[2], Luis Pereira[3], Julian S. Dean[4], Ian M. Reaney[4], Ana M. O. R. Senos[1], Paula M. Vilarinho[1*], J. Agostinho Moreira[2*]

[1] Department of Materials and Ceramic Engineering, CICECO – Aveiro Institute of Materials, University of Aveiro, 3810-193 Campus Santiago, Portugal
[2] IFIMUP, Institute of Physics for Advanced Materials, Nanotechnology and Photonics, Department of Physics and Astronomy of Faculty of Sciences, University of Porto, 4169-007 Porto, Portugal.
[3] CENIMAT-I3N, School of Science and Technology, FCT-NOVA, Universidade NOVA de Lisboa, Campus da Caparica. 2829-516 Caparica, Portugal
[4] Materials Science and Engineering, University of Sheffield, Sheffield S1 3JD, UK.

*Corresponding authors: paula.vilarinho@ua.pt, jamoreir@fc.up.pt

Abstract

Electric field and current applied to an unsintered ceramic body is known to promote low temperature and extremely fast densification, in a process referred to as FLASH sintering. Under the current urgency of the green transition of manufacturing processes, FLASH sintering is a very promising technology for materials industry. Suitable FLASH conditions result in dense ceramics but many issues associated with the effect of electric field and current on local chemistry, structure, and microstructure remain to be understood. We have used FLASH sintering to produce $K_{0.5}Na_{0.5}NbO_3$ (KNN), a lead-free compound suitable for piezoelectric applications. Using a combined X-ray diffraction and Raman spectroscopy study, here we show for the first time that, although the FLASH process may produce homogeneous ceramics with negligible concentration of secondary phase, macroscopic core-localized stresses remain which have significant consequences on the final properties of the sintered material. In addition, the internal stress state and its dependence on the local temperature during FLASH sintering are established by Finite Element Modelling (FEM). The identification of the fine structure of FLASH sintered materials is critical for

understanding the unique properties developed under this sintering process and for its development as an alternative low thermal budget sintering technology.

Key words:

FLASH sintering; Raman imaging; Finite Element Modelling; Stress state; Structure; Thermal gradient; Joule heating.

Introduction

FLASH is an electric field and current assisted densification technique for ceramics. This novel sintering process allows a considerable decrease in the processing time and temperature and thus it is considered a promising method to reduce the energy costs and environmental footprint associated with sintering [1], [2]. When an electric field is applied to a porous ceramic compact, no long-range current flow is observed. However, if the temperature is increased and/or enough defects are nucleated, a FLASH event occurs in which densification may take place in less than 60 s, depending on the field and current applied [3]. FLASH is one of a number of low energy sintering techniques such as Spark Plasma Sintering/Texturing (SPS/SPT) [4] and Cold Sintering Process (CSP) [5] which offer a path to reducing energy consumption within the ceramics industry.

In FLASH sintering, the ceramic is heated from the core to its surface by a Joule effect caused by an electric current imposed through surface mounted electrodes, typically metallic sheets. The appropriate operating conditions (e.g temperature, electric field, current density, time, atmosphere) have been reported to result in dense ceramics that are chemically and microstructurally uniform [6]–[8]. However, the rapidity of the FLASH event can induce non-equilibrium microstructures [9]. Thermal gradients [10], [11] and accelerated mass transport [2], together with non-uniform electric current distribution (hotspots) [12] and electromigration [13] are known to trigger microstructural [14], [15] and chemical [16] heterogeneity.

Although X-Ray Diffraction (XRD) has been used to study mechanisms that promote non-equilibrium phenomena [17]–[19], the structural and microstructural changes during FLASH are still not well understood. Here, we study FLASH sintering on Potassium Sodium Niobate, $K_{0.5}Na_{0.5}NbO_3$ (KNN), a lead-free ferroelectric with interesting functional properties [20], [21]. Undoped KNN is difficult to sinter conventionally due to K and Na volatilisation at high temperature [22] and alternative approaches, such as SPS/SPT [23], CSP [24] and FLASH [16], [25] are often sought. Our previous work demonstrated a particle-contact (size and shape) dependent sintering process [6], [26], [27]. Such contacts partially melt which allows particle sliding and pore removal [28]. While microstructural differences between FLASH and conventionally sintered KNN

ceramics are evident [16], [28], comparable electrical properties can be achieved by subsequent heat treatment [29].

Even though analysis of the macroscopic stresses has been reported for SPS and SPT, [23], [30], no such studies exist for FLASH sintering. While the occurrence of thermal gradients during FLASH process is an already reported phenomena [10], [31], [32], their consequences for the stress state of sintered ceramics remains unknown. In this work, Finite Element Modelling (FEM) is used to simulate the local temperature of a KNN ceramic during FLASH sintering. In parallel, XRD is performed to gain information on the overall structure and stress state of as-sintered ceramics, while Raman spectroscopy allows to assess the position-dependent structure, chemical composition and stress state of FLASH sintered KNN ceramics [33]. This unprecedent combination of techniques allows to comprehensively study the link between the local temperature during the FLASH sintering process and the resulting ceramics structure and microstructure, particularly focussing on their internal stress state.

Experimental

KNN powders were produced by a conventional solid-state route, and specimens obtained by uniaxial and isostatic pressing [6]. KNN ceramics were conventionally sintered 3 h at 1125 ºC, with heating and cooling rates of 5 ºC/min, in the absence of any electric field or current. Similarly, green compacts were FLASH sintered under Isothermal Conditions (I.C.) [6]. After an isothermal step of 30 min at 900 ºC, the electric field (300 V/cm) was applied, followed by an incubation time of ca. 60 s, and a current density rise to a limit of 20 mA/mm^2. Specimens were sintered in 60 s.

Scanning electron microscopy, SEM (*Hitachi SU-70*) was used to study the microstructure of dense ceramics. The sintered ceramics were grind and polished to approximately 2/3 of their initial thickness, to reveal their core (Figure S1). Polished ceramics were then etched 5 min, in 40 vol% HF, to reveal the grain structure. Polished ceramics were analysed by Electron Backscattered Diffraction Analysis (EBSD) and the average grain size ($\overline{G_{eq.}}$) determined from mapping more than 1000 grains [29]. For FLASH sintered ceramics, the regions immediately adjacent to the electrodes were not considered for microstructural

studies (ca. 1-2 mm each side). Density of ceramics was determined using the Archimedes method (in water) on at least three specimens.

Similarly polished sintered ceramics were analysed by X-Ray diffraction (XRD). A *PANalytical XPERT-PRO* diffractometer, using a Cu source ($K\alpha_1$ = 1.54060 Å), from 20 to 80º 2θ, with a step size of 0.026º and accumulation time of ca. 96 s, with a probe size of 1.4 mm in diameter was focused on the previously revealed ceramics' core. Lattice parameters were determined by Rietveld refinement of the experimental XRD data and were based on JCPDF 01-085-7128 file (KNN, A*mm2*). Residual stresses were estimated by XRD using different specimen tilt angles (Ψ), and by following equation 1, where k is the curve gradient of the normalized d-spacing (311 planes) vs. $\sin^2\Psi$, E is the Young modulus (104 GPa) and υ is the Poison ratio (0.27). 2θ from 70 to 80º was analysed since this contained the 311 reflection. For more details on the method, we refer the reader to refs [23], [34], [35]

$$\sigma_\phi = \left(\frac{E}{1+\nu}\right) k \quad (1)$$

Sintered and polished ceramics were further analysed by unpolarized micro-Raman single spot and imaging mode (schematics on Supplementary Information – Figure S1) using a Renishaw InViaTM Qontor® Confocal spectrometer operated with a 633 nm He-Ne laser line (power at 5 mW). Each Raman spectrum was acquired with an exposure time of 0.1 s and to achieve good spatial resolution for Raman imaging, ca. 290 000 spectra were collected for the 500 x 500 μm^2 maps, and 1 500 000 spectra for the 9 x 5 mm^2 maps. The pixel size varied from 1 to 30 μm^2, depending on the map area with a lateral resolution of 100 nm. The scattered light was analysed using an 1800 lines/mm diffraction grating, providing a spectral resolution better than 1.5 cm^{-1}. The frequency, linewidth, and intensity of the Raman bands were determined through best fit to a Lorentzian function.

COMSOL Multiphysics simulations were carried out to access the current density and temperature distribution in a monolithic KNN block. The model was based on the approach described in ref. [26]. Prior to simulation, the DC electrical conductivity of conventionally dense KNN ceramics was determined using a Keithley 2410 electrometer and the temperature dependence assigned to the material within the *COMSOL* software. An electric field of 300 V/cm was applied

across the model and scaled to the model size. The current flow (as a function of conductivity) and temperature were simulated at 1 s interval. As the electric field is being controlled, we monitor that the current in the simulation does not rise above the experimental limit of 20 mA/mm^2.

Results and discussion

Representative SEM micrographs of conventionally (Conv) and FLASH sintered KNN are shown in Figure 1 a) and b), respectively. Both ceramics exhibit a uniform density through the analysed region. A fine microstructure with uniform sized grains is depicted for FLASH ceramics, in Figure 1 b), while a coarser microstructure with abnormal grain growth is observed for conventionally sintered KNN (see Figure 1 a)). The average grain size is ~20% larger in conventionally than in FLASH sintered specimens (see average grain size, $\overline{G_{eq.}}$, in Table 1). Abnormal grain growth and secondary phases have been previously reported in conventionally sintered KNN [36], [37]. Chemical etching of conventionally sintered ceramics occurs differently from that of FLASH, with '*worm-like'* features within grains (Figure 1 a)), but classically etched grains in FLASH ceramics (Figure 1 b)). FLASH sintered specimens also showed evidence of grain pull out from the grinding, polishing and etching process which is attributed to the formation of mechanically and/or chemically unstable grain boundaries (GBs) [6]. More details on the microstructure of these ceramics can be found in reference 6 and supplementary information (Figure S2).

The respective structure and chemical composition of the ceramics were evaluated by EBSD analysis. Figure 1 c) and d) illustrate representative phase mapping for conventional and FLASH sintered specimens, respectively. The maps were obtained by indexing two crystalline phases: i) a $K_{0.5}Na_{0.5}NbO_3$ orthorhombic A*mm*2 perovskite phase, displayed with red colour, and ii) a $K_{0.8}Nb_5O_{15}$ (Nb-rich) tetragonal tungsten bronze structured secondary phase (P*4bm*) [23] and represented with green in Figure 1 c). For both samples, well defined grain boundaries are observed. The conventional ceramics clearly exhibit grains indexed according to $K_{0.8}Nb_5O_{15}$, with far fewer in FLASH sintered ceramics. Based on the area fraction of grains assigned to the secondary phase, the estimated concentration of $K_{0.8}Nb_5O_{15}$ (C_{sp}) in conventional KNN is 0.4 ± 0.1

vol% (Table 1). The relative density of FLASH and conventionally sintered ceramics are similar, within experimental error (Table 1). Chemical composition and microstructure non-uniformities between ceramics core and surfaces were not identified throughout several and systematic specimen analysis. Therefore, a uniform average density is considered.

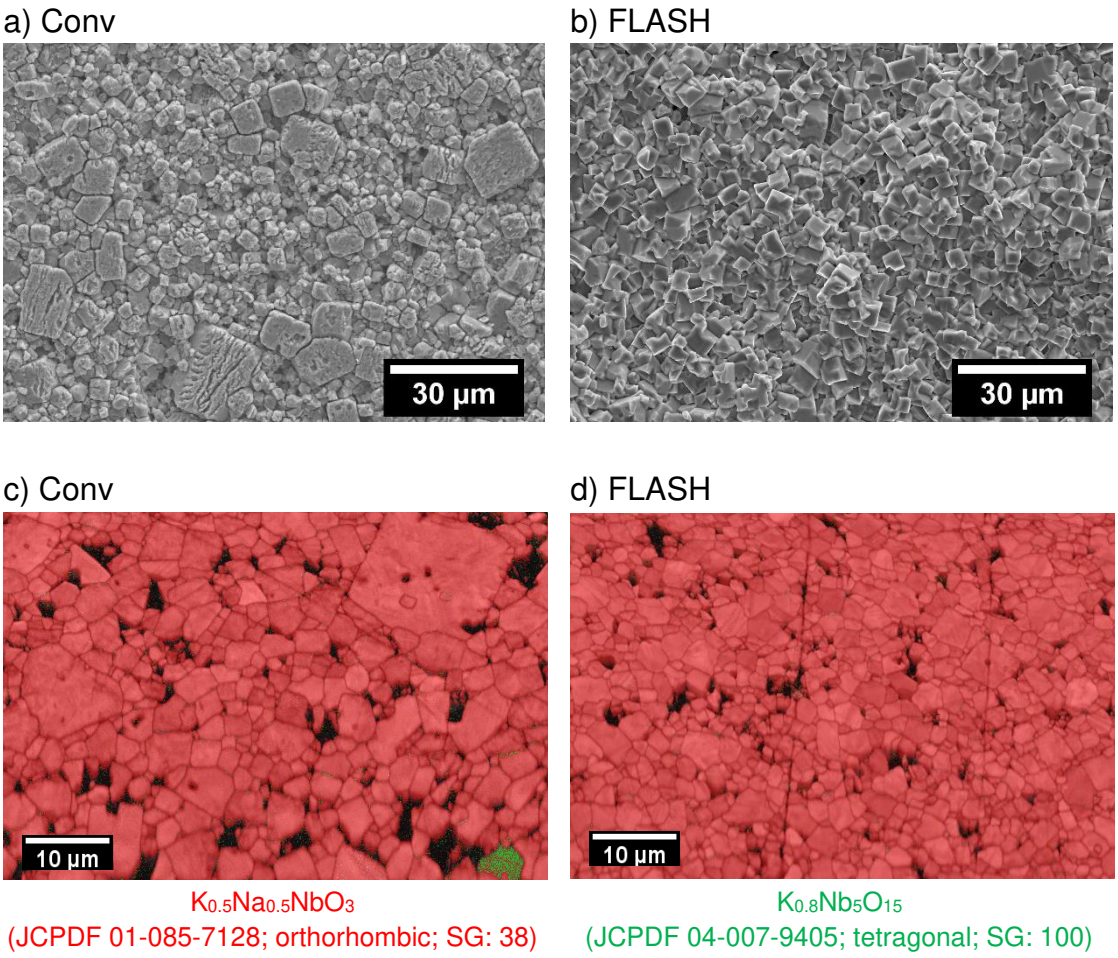

Figure 1 – SEM micrographs of a) FLASH and b) conventionally sintered KNN ceramics. EBSD phase maps are shown in c) and d), respectively. FLASH KNN presents a uniform grain size while conventionally sintered KNN exhibits some abnormal grain growth, together with more $K_{0.8}Nb_5O_{15}$ secondary phase.

Table 1 – Average equivalent grain size ($\overline{G_{eq.}}$), secondary phase concentration (C_{sp}) and relative density (ρ_{rel}) of conventionally and FLASH sintered KNN.

KNN	$\overline{G_{eq.}}$ (µm)	C_{sp} (vol.%)	$\rho_{rel.}$ (%)
Conv	1.77±0.05	0.4±0.1	96±2

FLASH	1.49±0.02	<0.05	93±3

Figure 2 a) shows representative XRD patterns of polished, as-sintered ceramics by FLASH and conventional sintering, respectively, recorded at room temperature from 20 - 80º 2θ. Qualitatively, the profile of the XRD patterns agree with the JCPDF file 01-085-7128, orthorhombic (A*mm2*) $K_{0.5}Na_{0.5}NbO_3$, previously indexed in EBSD data. The Rietveld refinement of the XRD data (presented in supplementary information, Figure S3) did not however, reveal the presence of secondary phases in conventional ceramics, suggesting the volume fraction is below the detection limit of the experimental equipment, which agrees with our C_{sp} estimation. The lattice parameters are shown in Table 2, and an isotropic volume decrease of the primitive cell is observed in FLASH (0.171%), compared with that of conventionally sintered ones.

The XRD estimated residual stress of the same polished as-sintered KNN ceramics is represented in Figure 2 b). The plot gives the normalized (311) interplanar spacing as a function of $\sin^2\Psi$, where Ψ is the sample's tilt angle [34]. For this purpose, different XRD patterns were recorded from 70 to 80º, at different tilt angle, resulting in residual stresses calculated from the slope of the linear dependences shown in Figure 2 b) [38]. The data slopes of both FLASH and conventionally sintered ceramics are negative, and because of those residual compressive stresses are estimated of -170±35 and -57±9 MPa, respectively. The compressive stress level of FLASH is, therefore more than 3 times greater than conventional KNN, with a larger dispersion.

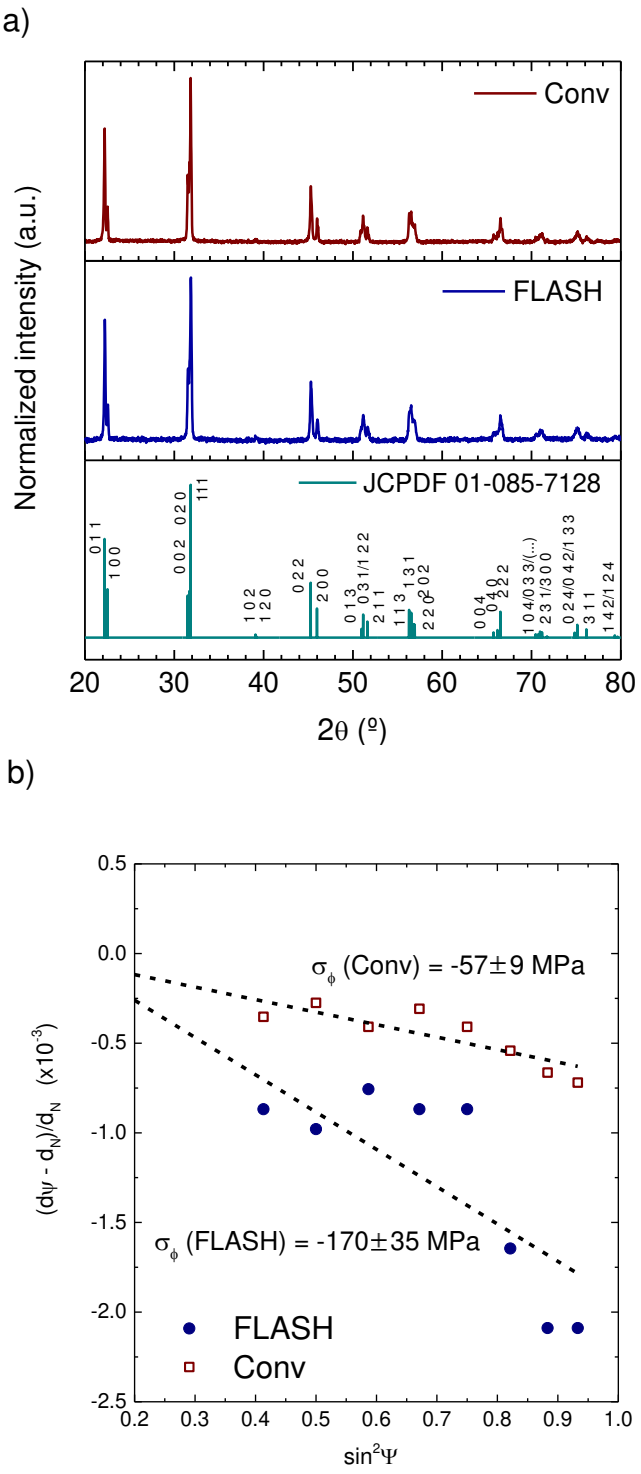

Figure 2 – a) X-ray diffraction patterns of $K_{0.5}Na_{0.5}NbO_3$ FLASH and conventional ceramics compared with JCPDF 01-085-7128 (perovskite orthorhombic structure, space group A*mm2*, $K_{0.5}Na_{0.5}NbO_3$). b) the d-spacing of (311) planes at different tilt angle Ψ normalized to "no tilt" d-spacing, versus the $\sin^2\Psi$ angle, and estimation of residual stresses on these ceramics.

Table 2 – Lattice parameters determined from the Rietveld analysis of the XRD patterns and respective unit cell volume (V). The unit cell volume variation is represented by $\Delta V = (V_{FLASH} - V_{Conv})/V_{Conv}$.

	Lattice parameter (Å)			V (Å^3)	ΔV (%)
Specimen	a	b	c		
Conv	3.944(6)	5.645(1)	5.675(4)	126.378	-0.171
FLASH	3.941(9)	5.642(8)	5.671(9)	126.162	

To establish the link between the sintering, local/internal stresses and structural/chemical changes in ceramics, spatially resolved data, such as that generated from micro-Raman imaging, is demanded. The representative unpolarized Raman spectra of FLASH and conventional KNN, recorded at room conditions in the 100 – 1000 cm^{-1} spectral range, are illustrated in Figure 3 a). The Raman profiles agree with the ones previously reported for KNN [30], [39], with the same spectral profile in FLASH and conventional ceramics, corroborating XRD data. Factor group analysis for the Γ-point Raman active modes of the orthorhombic phase (space group A*mm2*) is:

$$\Gamma^{opt} = 4A_1 + 4B_1 + 3B_2 + A_2 \quad (2)$$

The Raman signature is characterized by two main spectral regions, which are assigned to different vibrational modes. The bands observed between 100 and 180 cm^{-1} are assigned to translation modes of K^+ and Na^+ cations [39], and those from 180 to 1000 cm^{-1} to bending and stretching vibrations of the NbO_6 octahedra [39]. According to Kakimoto *et al.* [39], the vibrational modes υ_1 to υ_3 are stretching modes, while υ_4 and υ_5 are assigned to the bending modes of the NbO_6 octahedra. The atomic displacements associated to each NbO_6 vibration are schematically represented in Figure 3 b).

a)

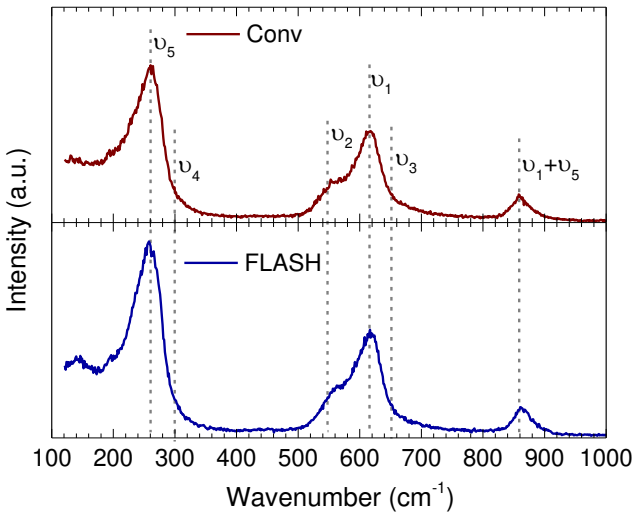

b)

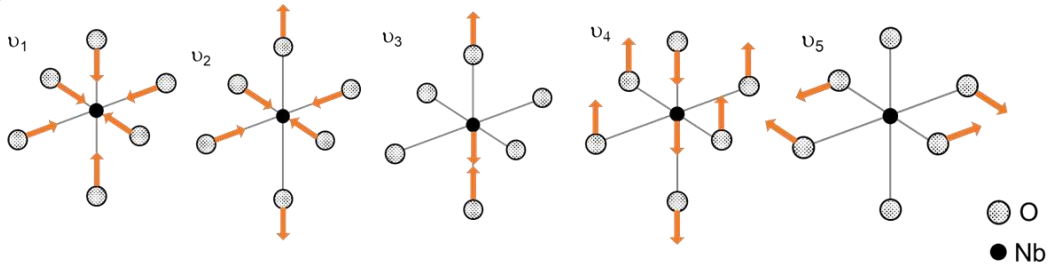

Figure 3 – a) Unpolarized Raman spectra of conventionally (Conv) and FLASH sintered ceramics with mode assignment. b) Schematic representation of internal vibrational modes of NbO_6 octahedra (adapted from [39]); υ_1 and υ_2 are stretching modes and υ_3 to υ_5 are bending modes.

Among the Raman-active modes, we will focus our attention on the symmetrical stretching mode υ_1 and the bending mode υ_5: υ_1 is characteristic of octahedral distortions, as its frequency depends on the mean Nb-O bond length, following Badger's rule [40], [41], while υ_5 involves the octahedral bending vibration and is sensitive to the shear strain. Both modes therefore, give insight regarding the relation of residual stress to structural distortions. However, the accurate determination of the υ_5 mode frequency through spectral deconvolution of the spectral range where this band is observed is hindered by strong overlap with other modes. To overcome this handicap, we have focused our attention on the band located at 860 cm^{-1}, which is assigned to the second-order mode $\upsilon_1+\upsilon_5$.

To gain insight into the relation of sintering with the structural distortions of the KNN ceramics, we performed a detailed micro-Raman imaging study at room temperature on the polished surface of as-sintered ceramics. Figure 4 a) gives the optical microscope image of the FLASH sintered ceramics. The positive electrode area is visible on the left, adjacent to the area used for characterization (e.g. in microstructure analysis) and the negative electrode contact is revealed on the right. These areas are highlighted as 1 and 5 for positive and negative electrodes, respectively, 2, 3 and 4 for zones in a straight line between electrodes (specimen core) and 6 and 7 for the top and bottom surfaces. Figure 4 b) includes the representative unpolarized Raman spectra recorded at the locations identified by the numbered spots in Figure 4 a). The Raman spectral profile is not strongly dependent of the position on the FLASH ceramic (core, surface or electrodes) but does reveal sintering dependent structural distortions.

The bands of interest for analysis are highlighted with colours in spectra of Figure 4 b) and are magnified in detail in c). For comparison, the wavenumber (ω_a) of each relaxed mode was considered at 615 (υ_1) and 859 ($\upsilon_1+\upsilon_5$) cm^{-1}, as reported independently for single crystals [42], [43] and ceramics [30], [39], [44]. These are indicated in Figure 4 c) by the vertical dashed blue lines, and the ω_a shifts, relative to the assumed reference values, for υ_1 and $\upsilon_1+\upsilon_5$ bands, are revealed. The corresponding Raman images, weighted to the position of the Raman mode, are presented in Figure 4 d) and e) for υ_1 and $\upsilon_1+\upsilon_5$, respectively. The frequency of both υ_1 (d) and $\upsilon_1+\upsilon_5$ (e) modes is position dependent as revealed by a significant wavenumber shift ranging from 612 to 622 and 856 to 866 cm^{-1} (10 cm^{-1}), respectively. In both analyses, a significant upshift in the positive electrode (1) that corresponds to 6 to 7 cm^{-1} above the reference value is observed, followed by an upshift at the ceramic core (numbers 2 to 5) of 5 to 6 cm^{-1}. Although a slight downshift is observed at the surfaces (6 and 7) of 1 to 2 cm^{-1}, the majority of the specimen presents a υ_1 and $\upsilon_1+\upsilon_5$ upshift. Following Badger's rule (eq. 2) [40], [41] as the length of Nb-O bond (d_{Nb-O}) is decreased (indicating a volume reduction of the Nb-O octahedra), ω_a is augmented.

$$\omega_a \propto \frac{1}{d_{Nb-O}^{\frac{3}{2}}} \quad (2)$$

In accordance with equation 2 and Figure 4, the core areas of FLASH ceramics (corresponding to numbers 1 to 5 in Figure 4 b)) present a shorter Nb-O bond; the opposite occurs for the surfaces (numbers 6 and 7) of the FLASH ceramic but with a lower intensity. Nonetheless, an estimation of variation in d_{Nb-O} with respect to the reported ω_a values (Figure 4) gives a maximum bond length variation of ~ - 1% at the core and + 0.5% at the surfaces. This observation agrees with the overall primitive cell compression and the residual compressive stresses found in XRD data of FLASH ceramics but suggests a non-uniform distribution of the stresses in the FLASH KNN, not identified by XRD. The non-uniform stress distribution between the positive and negative electrodes is related with the previously reported increase in local temperature of the positive side during the FLASH [10].

To understand the non-uniform distribution of residual stresses on as-sintered FLASH ceramics, Finite Element Modelling (FEM) was used to simulate the temperature distribution in the KNN specimens during FLASH sintering. The results of simulated current density and respective temperature distribution profiles evolving as a function of time are represented in Figure 5. The current density increases with time which, due to the overall heating of the system (by Joule effect), is uniformly distributed throughout the KNN body. In contrast, the temperature distribution at each stage is inhomogeneous. The temperature increase by Joule effect occurs through the specimen core towards its surface. It should be noted that at the transition from t = 5 to t = 6 s, the simulation is no longer representative of the experimental setup, as the experimental current limit (20 mA/mm^2) is exceeded and therefore, t = 5 s was selected for comparison with the Raman imaging data in Figure 4 f).

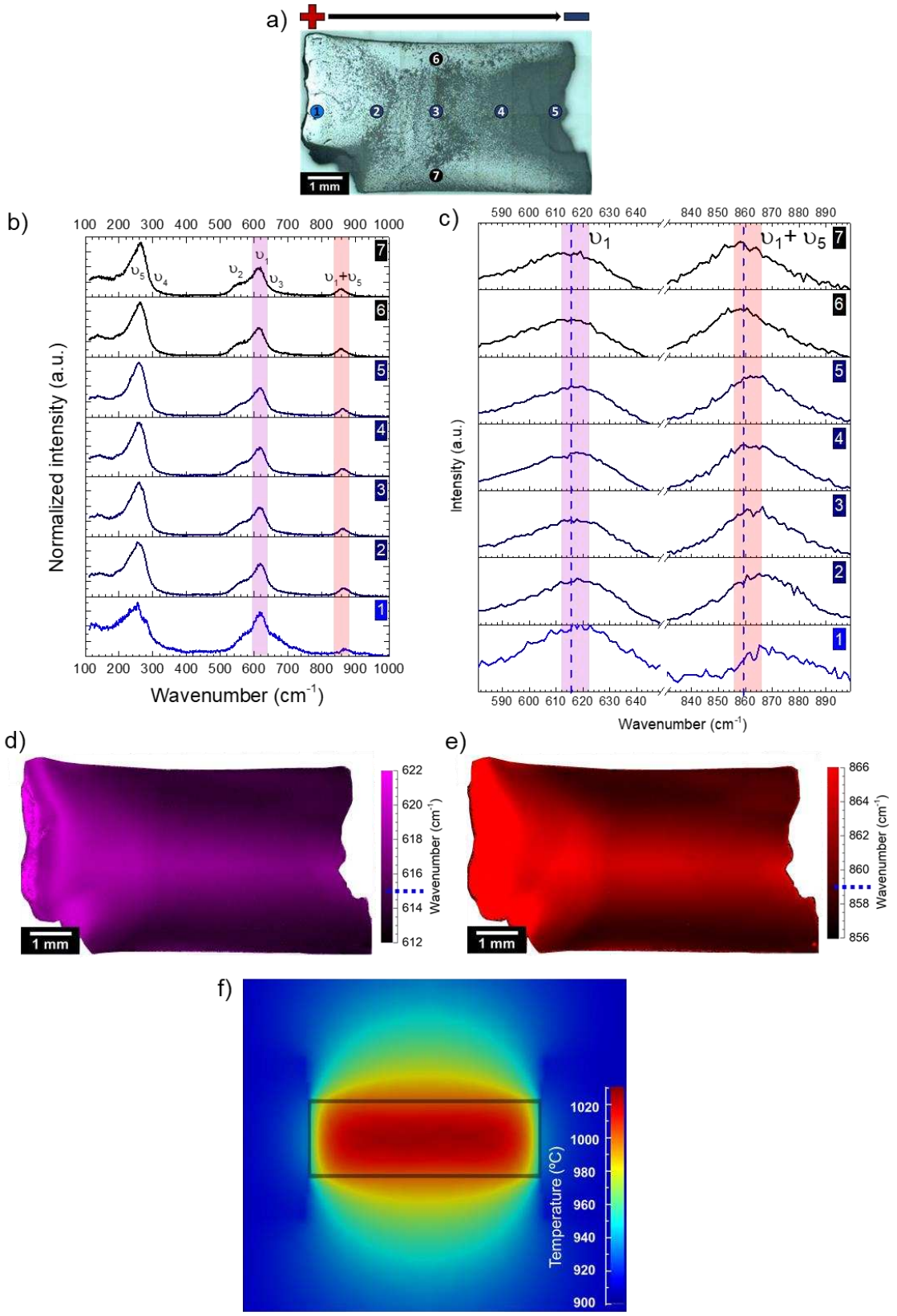

Figure 4 – a) optical microscope image of FLASH ceramic; b) Raman spectra of correspondent spots 1 to 7 identified in a); c) magnification of b) for Raman modes of interest; Raman spectroscopy imaging for the peak position (wavenumber) fitted for d) υ_1 in purple and e) $\upsilon_1 + \upsilon_5$ in red; pixel size ≈ 30 μm^2. f) FEM simulation of temperature distribution during FLASH sintering; the surfaces of the simulated KNN block of material are represented by the grey rectangle.

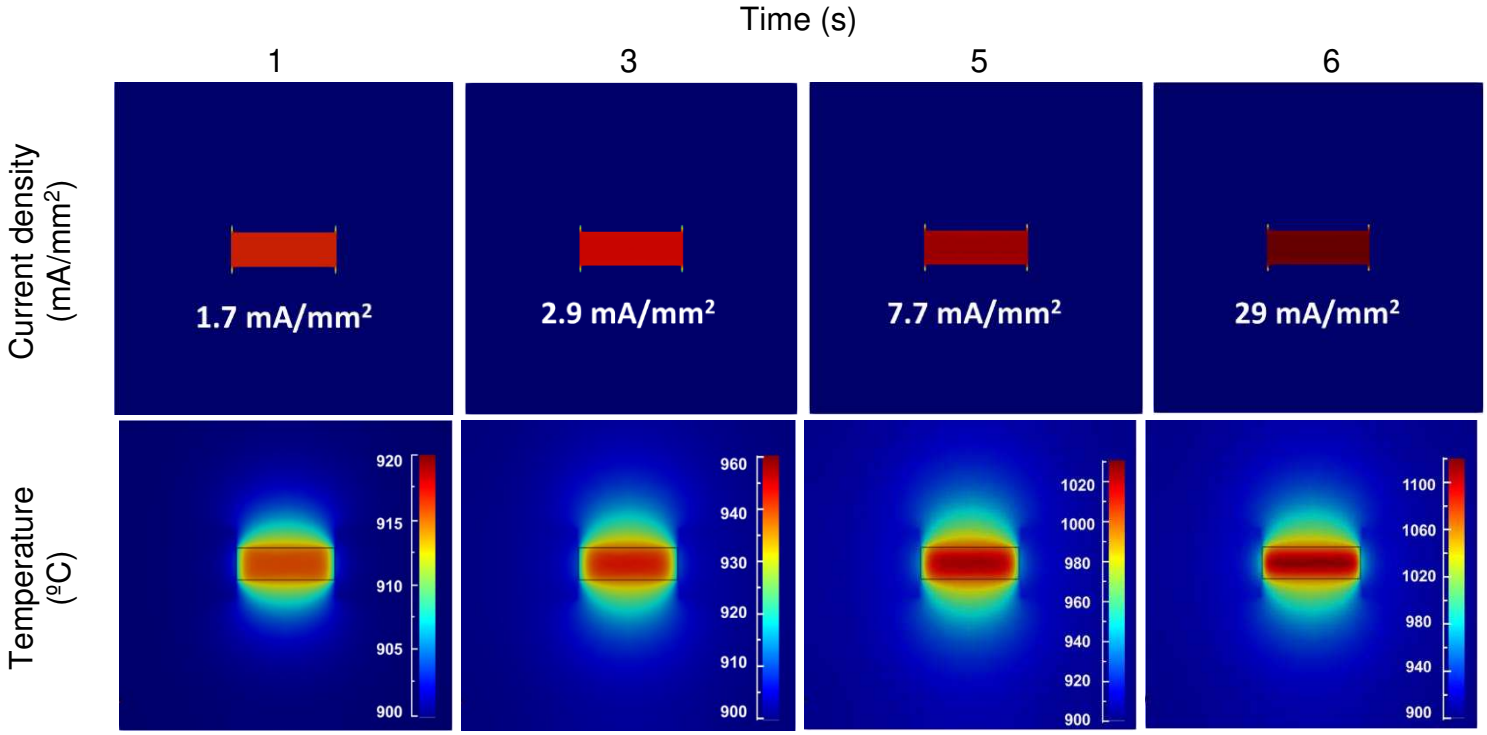

Figure 5 – Simulated current density (top) and temperature (bottom) distribution for simulation times of 1, 3, 5 and 6 seconds after the starting simulation condition: equilibrium temperature of 900 ºC. For clarity, the surface of KNN block is represented by a grey rectangle in the temperature representations. At t = 6 s, the experimentally imposed current density limit of 20 mA/mm^2 is exceeded and the simulation is no longer valid.

The simulated temperature distribution through the KNN modelled specimen (delineated by the grey rectangle in Figure 4 f)) during the FLASH reveals a spatial temperature dependence on the ceramic. The lack of positive/negative discrimination in the model results in the absence of asymmetries between those in the simulated temperature. On the other hand, at the core of the modelled ceramic, ≈1030 ºC is achieved, while at the surface, the temperature drops to <1000 ºC. Due to thermal dissipation, the surroundings of the ceramic are at a temperature close to that of the furnace (900 ºC). The Raman imaging schemes (Figure 4 d), e)) and FEM simulation (Figure 4 f)) show agreement between the local KNN structure and the simulated temperature profile, respectively. A link between local temperature during FLASH and local structure in sintered ceramics is therefore evidenced, with the higher temperature at the core of the ceramics during FLASH sintering being related with a Nb-O

bond decrease, equivalent to a unit cell compression. On the other hand, tensile stresses are present at the ceramic's surfaces.

To validate if the stress state of FLASH sintered ceramics is a feature of the sintering process, a conventionally sintered ceramic was studied. Figure 6 a) presents a representative Raman spectroscopy image weighted on the $\upsilon_1+\upsilon_5$ mode wavenumber. For comparison, the core area of the FLASH ceramic was analysed under the same experimental conditions as used for conventional ceramics and is revealed in b). Micro-Raman images were acquired at the core of conventionally (a) and FLASH (b) sintered ceramics. Whereas FLASH ceramic (b) demonstrates a very uniform dependence of ω_a along all the analysed area, with a strong upshift from ω_a = 859 cm^{-1}, as shown in Figure 4 a) (corresponding to pin number 3 area), conventional ceramic (a) presents an overall lower ω_a, closer to the reported value [39].

However, conventional ceramic presents micron-sized non-uniformities, characterized by localized strong upshifts, highlighted with circles and the respective number 2. The uniform and representative zones in the ceramic are identified with the number 1. The Raman spectra of areas 1 and 2 are represented in Figure 6 c). While a typical KNN Raman spectrum is depicted for 1, indicating that such areas do not present any relevant structural or chemical dissimilarity, the same is not true for spectrum 2, where there is an anomaly in the background, with spurious bands being revealed (identified with *). These observations in conventionally sintered ceramics may be explained by the presence of the Nb-rich secondary phase, previously identified in EBSD (Figure 1), or the contribution of polishing residues trapped in pores.

If the Raman modes with upshift in conventional ceramics are representative of secondary phases, such high concentration would result in secondary reflections in XRD patterns, since their volume fraction would be above the typical detection limit. Therefore, the presence of polishing impurities seems more plausible, which is consistent with the similar electrical properties of conventionally and FLASH sintered ceramics, obtained after post-sintering heat treatment [29].

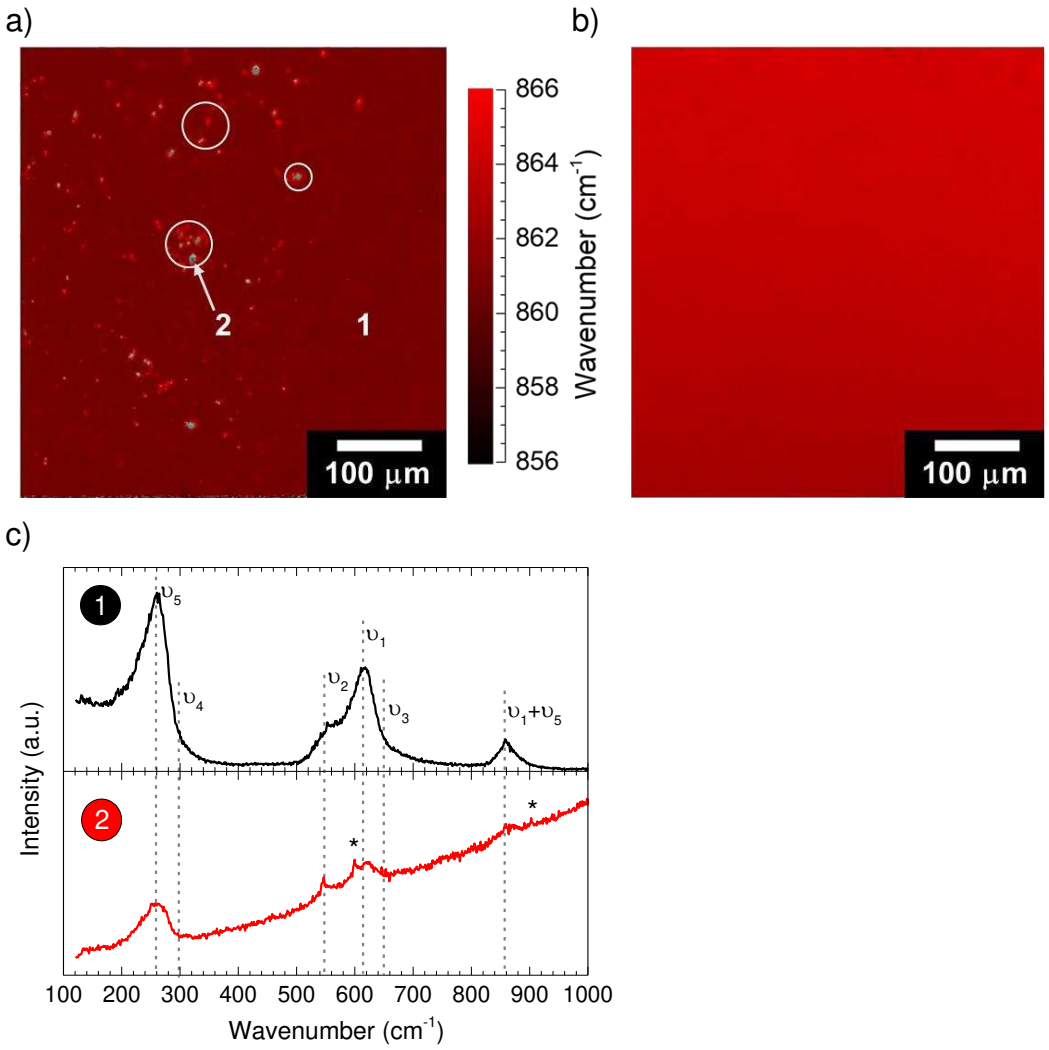

Figure 6 – Raman spectroscopy imaging on the mode at ca. 860 cm^{-1} of a) conventionally and b) FLASH sintered ceramics; pixel size = 1 μm^2. c) Respective Raman spectra for positions 1 and 2 in conventional ceramic's map, with identification of spurious peaks (*).

It is therefore demonstrated that the strong core-located Raman frequency upshift of bands assigned to υ_1 and $\upsilon_1+\upsilon_5$ modes in FLASH ceramics, associated with compressive stresses, is a feature (like a fingertip) of the sintering process, as suggested by the relationship between local simulated temperature and residual stresses in the KNN ceramics (Figure 4). The agreement between local Raman and temperature gradients leaves no room for doubt about the stress state of the as-sintered ceramics and its origin. We propose the following hypothesis to explain such observations. During FLASH sintering, there is an inhomogeneous temperature distribution, schematically represented in Figure 7

a), of the KNN ceramic (Figure 4 and Figure 5). We assume that the temperature gradient is kept throughout the FLASH process and that the specimen acts as a resistance, being heated through its core and dissipating heat to the surrounding environment through the surfaces. Therefore, there is a non-uniform expansion of the KNN unit cell, that is larger at the core in comparison to its surface. Consequently, tensile stresses at the surface are developed due to thermal expansion. However, the core, which would experience a larger thermal expansion than the surface, is under compression since it is surface-constrained by the cooler outer regions. The combined representation of temperature and stress development as a function of the specimen depth (OY axis) is shown in Figure 7 b). We propose that this stress distribution as a function of the ceramic surface position is then locked-in during fast cooling once the electric current is terminated. Therefore, as the surface fraction that dissipates the heat is significantly smaller in volume than the core, an overall compressive stress-state is left in the ceramic, as identified by XRD residual stress analysis. It is not argued that stress relaxation does not occur during cooling after the FLASH; however, it is most certainly not complete as the stress-dependence is spatially resolved by Raman, with compressive and tensile stresses observed at the ceramic core and surfaces, respectively.

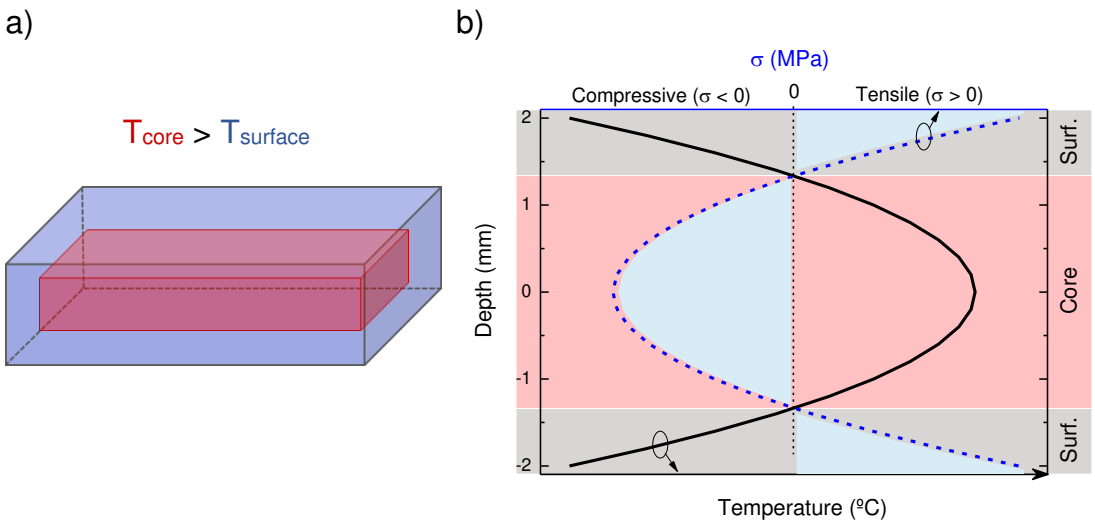

Figure 7 – a) schematic representation of temperature distribution of the KNN ceramic during FLASH sintering and b) graphical illustration of the compressive and tensile stresses at the core and surface, respectively (with dashed blue line and blue shadowed areas), as the consequence of the temperature gradient (black solid line).

If we compare the proposed mechanism for stress development during FLASH sintering with a classic quench process, tensile stresses are typically located at the core with the surface under compression. This is due to two major factors, (i) in quenching stresses are developed during the cooling of a thermally equilibrated part and (ii) parts are heated from the surroundings towards the core [45], [46]. In the proposed mechanism for stress development during FLASH sintering, stresses are developed during heating from the core towards the surface, which does not allow temperature equilibration and the associated stresses become locked-in during the extremely fast cooling from high temperature FLASH state to the furnace temperature. Further stress release might occur during the furnace cooling from ~900 ºC to room temperature. However, our observations indicate that such stress release is not significant to the overall stress state of as-sintered ceramics.

This work shows that significant residual stresses are present in as-FLASH sintered KNN ceramics which may affect their electromechanical performance. The post processing heating step of FLASH sintered ceramics, e.g. associated with the application and cure of metallic electrodes [29] is typically associated with stress release and relaxation. Analysis by X-ray diffraction on a 900 ºC - 1 h heat treated FLASH ceramic did not reveal relevant residual stresses. Therefore, thermal relaxation of FLASH ceramics is a topic requiring further exploration.

The superior electromechanical properties of KNN ceramics produced by FLASH sintering, at lower temperature, when compared with conventional process, are related with the lower content of secondary phase and final stress level of FLASH KNN. Systematic characterization of the dielectric, piezoelectric, and ferroelectric properties of these ceramics are the subject of another manuscript under revision [47].

Conclusion

This study reveals that FLASH sintering induces stresses in the densified ceramics. By combining the overall structural and microstructural analysis provided by EBSD and XRD with Raman spectroscopy and FEM simulations of the FLASH sintering process, the relationship between densification and internal

stresses in KNN ceramics was established. Conventional sintering gives macroscopic homogeneous ceramics but with a low volume fraction of secondary phase. The FLASH process produces a microscopically homogeneous ceramic with even less secondary phases than conventional but macroscopic compressive stresses are present in the specimen core. The proposed mechanism for the development of stresses during FLASH sintering is consistent with the decrease in cell volume and higher residual compressive stresses compared to conventional ones observed by XRD.

Acknowledgements

The authors give a special acknowledgment to Artur Sarabando and Dr. Rosário Soares for the data acquisition and analysis of residual stress evaluation by XRD. To Dr. Alex Tkach for the discussion of XRD data. This work was developed within the scope of the projects CICECO-Aveiro Institute of Materials, UIDB/50011/2020 & UIDP/50011/2020, financed by national funds through the FCT/MEC and when appropriate co-financed by FEDER under the PT2020 Partnership Agreement and from IFIMUP, with ref. NORTE-01-0145-FEDER-022096 & UID/NAN/50024/2019. Additionally, the work was financed by Portugal 2020 through European Regional Development Fund (ERDF), in the frame of Operational Competitiveness and Internationalization Programme (POCI), in the scope of the project “FLASH sintering of lead free functional oxides towards sustainable processing of materials for energy and related applications - FLASH”, POCI-01-0247-FEDER-029078. Ricardo Serrazina and Mariana Gomes acknowledge the financial support of, respectively, FCT (SFRH/PD/BD/128411/2017) and the project PTDC/NAN-MAT/28538/2017.

Supplementary information

Figure S1 shows a schematic of the polishing process of as-sintered conventional and FLASH ceramics in a) and the respective surface of analysis in b). Approximately one third to one half of the ceramic thickness was removed (stripes in the figure) by polishing with SiC paper. The final polishing was performed with a P4000 paper, equivalent to a grain size of ≈ 5 μm. After polishing, specimens were washed in ethanol under sonication. The dried ceramics were then analysed by X-ray diffraction and Raman spectroscopy using single spot and imaging mode.

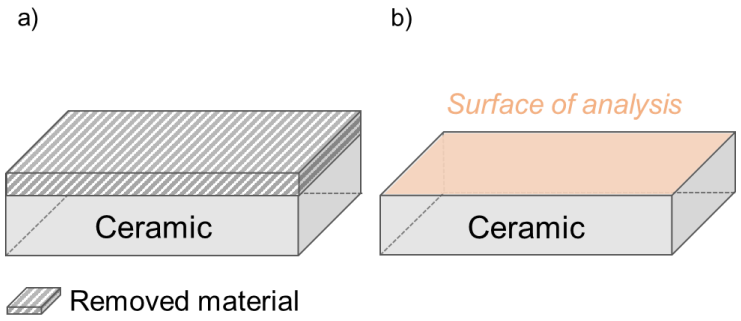

Figure S1 – Schematic representation of a) polishing process with indication of removed material and b) the revealed surface for X-ray diffraction, SEM and Raman spectroscopy analysis. The polishing step allowed the central part of the ceramics (core) to be simultaneously revealed with their surface.

More details on the microstructure of these ceramics can be found in reference 6 and supplementary information Figure S2.

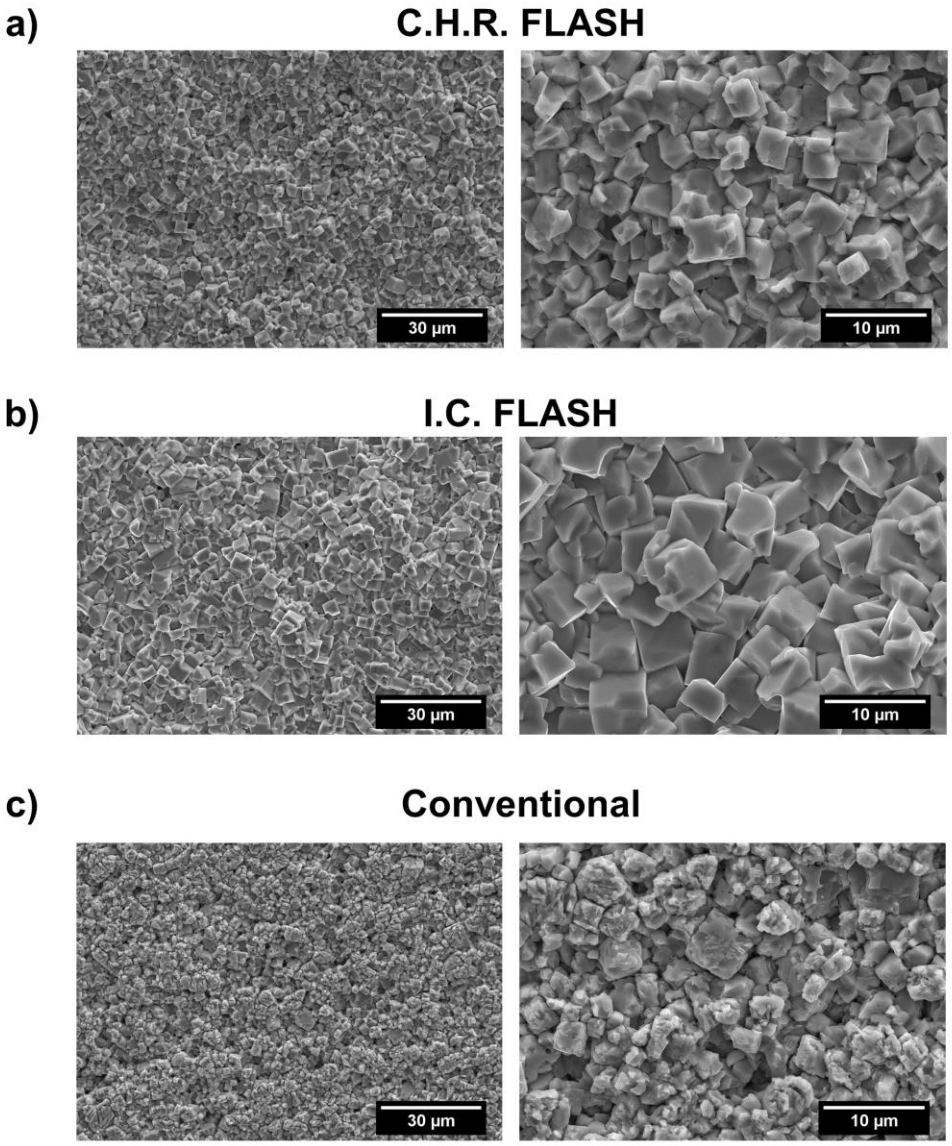

Figure S2 – Scanning electron microscopy (SEM) micrographs of a) C.H.R. FLASH, b) I.C. FLASH and c) conventionally sintered KNN ceramics, acquired with a 15 keV accelerating voltage at different magnifications, 1000 and 3000 times, left and right, respectively, *from [6] R. Serrazina, A. M. O. R. Senos, L. Pereira, J. S. Dean, I. M. Reaney, and P. M. Vilarinho, "The Role of Particle Contact in Densification of FLASH Sintered Potassium Sodium Niobate," Eur. J. Inorg. Chem., vol. 2020, no. 39, pp. 3720–3728, 2020.*

a)

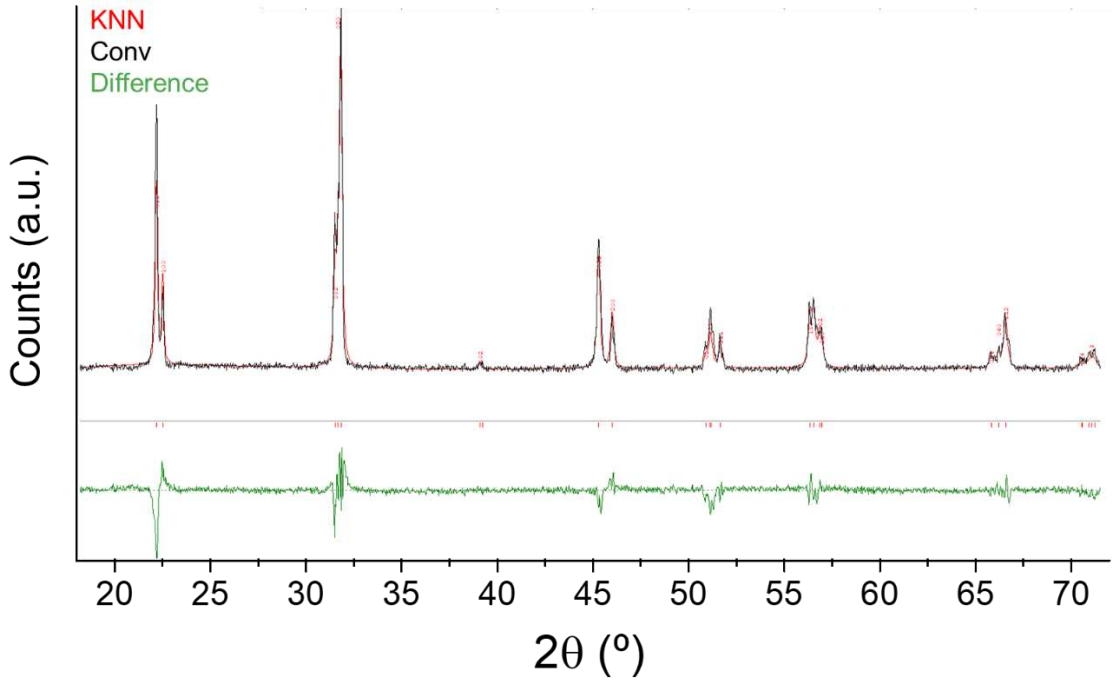

b)

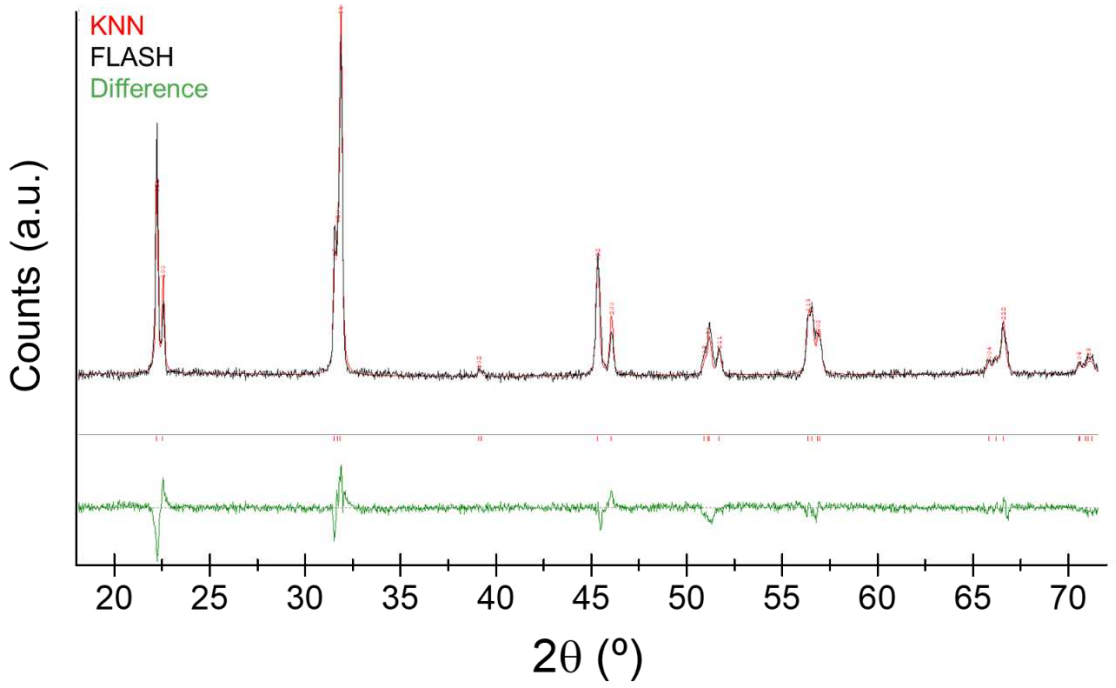

Figure S3 – Rietveld refinement results of XRD analysis of a) conventionally and b) FLASH sintered KNN. The black curve shows the experimentally obtained diffraction pattern, the red curve is the calculated pattern and the green curve reveals the difference.

COMSOL Multiphysics was used to develop the Finite Element Model for the simulation of both current density distribution and respective temperature (due to heating by Joule effect). [26]. The DC electrical conductivity of conventional KNN ceramics was accessed using a Keithley 2410 electrometer, with a 1 V/cm applied electric field. Platinum electrodes were painted and sintered on opposite faces of the ceramics prior to measurement. A constant heating rate of 10 ºC/min up to 1000 ºC was employed and the conductivity as a function of temperature is shown in Figure S4. The electrical conductivity of KNN was subsequently extrapolated for T > 1000 ºC based on an Arrhenius fit to the data. Measurements on several different conventionally sintered ceramics were performed, and the results were consistent and considered to be representative of KNN ceramics.

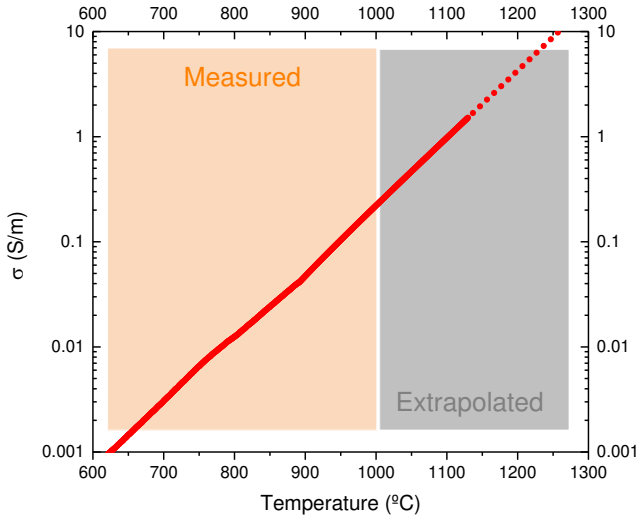

Figure S4 - Measured KNN conductivity σ (S/m) over measured temperature (with a 10 ºC/min heating rate) under an applied electric field of 1 V/cm.

To simulate the FLASH process, the sample holder and respective green KNN compact were described, as shown in Figure S5. For simulation, the green compact was approximated to a single 15 x 5 mm^2 monolithic block of material, identified as *KNN* in Figure S4. Thickness was not considered as only a 2D model was developed. The bi-dimensional approximation allows faster simulation times without compromising the results. KNN (with the respective electrical conductivity) was modelled to establish a perfect contact with two opposite

platinum electrodes, that were also in contact with alumina parts, as in the experimental setup [28].

The FLASH process simulation was achieved using a *Terminal* function to one electrode, and a *Ground* function to the opposite electrode. A 300 V/cm electric field was scaled to the *terminal-ground* functions and the current was calculated and simulated as with respect to temperature and conductivity. To allow heat dissipation, the modelled setup was considered to be in air. Alumina electrical conductivity was taken as constant (10^{-12} S/m), while the thermal conductivity of KNN and alumina was considered temperature dependent and equal to 2.6 W/(m.K) and 27 W/(m.K), respectively. The time dependent model was run at a starting temperature of 900 ºC, representative of furnace equilibrium temperature before the application of the electric field. The results of current density and temperature profile were recorded at 1 s time intervals and are shown in Figure 5.

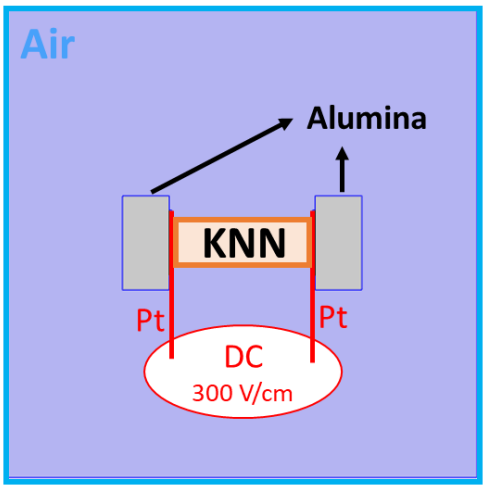

Figure S5 - Schematic representation of the model.

References

[1] C. E. J. Dancer, “Flash sintering of ceramic materials,” Mater. Res. Express, vol. 3, no. 10, pp. 102001–102025, 2016.

[2] M. Biesuz, S. Grasso, and V. M. Sglavo, “What’s new in ceramics sintering? A short report on the latest trends and future prospects,” Curr. Opin. Solid State Mater. Sci., vol. 24, no. 5, p. 100868, 2020.

[3] M. Biesuz and V. M. Sglavo, “Flash sintering of ceramics,” J. Eur. Ceram. Soc., vol. 39, no. 2–3, pp. 115–143, 2019.

[4] O. Guillon et al., “Field-assisted sintering technology/spark plasma sintering: Mechanisms, materials, and technology developments,” Adv. Eng. Mater., vol. 16, no. 7, pp. 830–849, 2014.

[5] J. Guo et al., “Cold Sintering: Progress, Challenges, and Future Opportunities,” Annu. Rev. Mater. Res., vol. 49, no. 1, pp. 275–295, 2019.

[6] R. Serrazina, A. M. O. R. Senos, L. Pereira, J. S. Dean, I. M. Reaney, and P. M. Vilarinho, “The Role of Particle Contact in Densification of FLASH Sintered Potassium Sodium Niobate,” Eur. J. Inorg. Chem., vol. 2020, no. 39, pp. 3720–3728, 2020.

[7] D. Liu, Y. Gao, J. Liu, Y. Wang, and L. An, “Effect of holding time on the microstructure and properties of flash-sintered Y2O3-doped ZrO2,” Ceram. Int., vol. 42, no. 15, pp. 17442–17446, 2016.

[8] L. A. Perez-Maqueda, E. Gil-Gonzalez, A. Perejon, J. M. Lebrun, P. E. Sanchez-Jimenez, and R. Raj, “Flash sintering of highly insulating nanostructured phase-pure BiFeO3,” J. Am. Ceram. Soc., vol. 100, no. 8, pp. 3365–3369, 2017.

[9] J. V. Campos et al., “Flash sintering scaling-up challenges: Influence of the sample size on the microstructure and onset temperature of the flash event,” Scr. Mater., vol. 186, pp. 1–5, Sep. 2020.

[10] M. Biesuz et al., “Investigation of electrochemical, optical and thermal effects during flash sintering of 8YSZ,” Materials (Basel)., vol. 11, p. 1214, 2018.

[11] J. G. Pereira Da Silva, J. M. Lebrun, H. A. Al-Qureshi, R. Janssen, and R. Raj, “Temperature Distributions during Flash Sintering of 8% Yttria-Stabilized Zirconia,” J. Am. Ceram. Soc., vol. 98, no. 11, pp. 3525–3528,

2015.

[12] M. S. Bernardo, T. Jardiel, A. C. Caballero, M. Bram, J. Gonzalez-Julian, and M. Peiteado, “Electric current activated sintering (ECAS) of undoped and titanium-doped BiFeO3 bulk ceramics with homogeneous microstructure,” J. Eur. Ceram. Soc., vol. 39, no. 6, pp. 2042–2049, 2019.

[13] W. Rheinheimer, X. L. Phuah, H. H. Wang, F. Lemke, M. J. Hoffmann, and H. H. Wang, “The role of point defects and defect gradients in flash sintering of perovskite oxides,” Acta Mater., vol. 165, pp. 398–408, 2019.

[14] W. Qin, H. Majidi, J. Yun, and K. van Benthem, “Electrode Effects on Microstructure Formation During FLASH Sintering of Yttrium-Stabilized Zirconia,” J. Am. Ceram. Soc., vol. 99, no. 7, pp. 2253–2259, 2016.

[15] Y. Zhang, J. Il Jung, and J. Luo, “Thermal runaway, flash sintering and asymmetrical microstructural development of ZnO and ZnO-Bi2O3 under direct currents,” Acta Mater., vol. 94, pp. 87–100, 2015.

[16] G. Corapcioglu, M. A. Gulgun, K. Kisslinger, S. Sturm, S. K. Jha, and R. Raj, “Microstructure and microchemistry of flash sintered K0.5Na0.5NbO3,” J. Ceram. Soc. Japan, vol. 124, no. 4, pp. 321–328, 2016.

[17] S. K. Jha et al., “The effects of external fields in ceramic sintering,” J. Am. Ceram. Soc., vol. 102, no. 1, pp. 5–31, 2019.

[18] H. Charalambous, S. K. Jha, R. T. Lay, A. Cabales, J. Okasinski, and T. Tsakalakos, “Investigation of temperature approximation methods during flash sintering of ZnO,” Ceram. Int., vol. 44, no. 6, pp. 6162–6169, Apr. 2018.

[19] J. M. Lebrun et al., “In-situ measurements of lattice expansion related to defect generation during flash sintering,” J. Am. Ceram. Soc., vol. 100, no. 11, pp. 4965–4970, 2017.

[20] J. Rödel, K. G. Webber, R. Dittmer, W. Jo, M. Kimura, and D. Damjanovic, “Transferring lead-free piezoelectric ceramics into application,” J. Eur. Ceram. Soc., vol. 35, no. 6, pp. 1659–1681, 2015.

[21] H. Sun, J. Liu, X. Wang, Q. Zhang, X. Hao, and S. An, “(K,Na)NbO3 ferroelectrics: a new class of solid-state photochromic materials with reversible luminescence switching behavior,” J. Mater. Chem. C, vol. 5, pp. 9080–9087, 2017.

[22] J. Pavlič, B. Malič, and T. Rojac, “Microstructural, structural, dielectric and

piezoelectric properties of potassium sodium niobate thick films," J. Eur. Ceram. Soc., vol. 34, no. 2, pp. 285–295, 2014.

[23] R. Pinho et al., "Spark plasma texturing: A strategy to enhance the electro-mechanical properties of lead-free potassium sodium niobate ceramics," Appl. Mater. Today, vol. 19, p. 100566, 2020.

[24] J. Ma et al., "Composition, microstructure and electrical properties of K0.5Na0.5NbO3 ceramics fabricated by cold sintering assisted sintering," J. Eur. Ceram. Soc., vol. 39, no. 4, pp. 986–993, 2019.

[25] Y. Wu, X. Su, G. An, and W. Hong, "Dense Na0.5K0.5NbO3 ceramics produced by reactive flash sintering of NaNbO3 - KNbO3 mixed powders," Scr. Mater., vol. 174, pp. 49–52, 2020.

[26] R. Serrazina, P. M. Vilarinho, A. M. O. R. Senos, L. Pereira, I. M. Reaney, and J. S. Dean, "Modelling the particle contact influence on the Joule heating and temperature distribution during FLASH sintering," J. Eur. Ceram. Soc., vol. 40, pp. 1205–1211, 2020.

[27] R. Serrazina, C. Ribeiro, M. E. Costa, L. Pereira, P. M. Vilarinho, and A. M. O. R. Senos, "Particle characteristics influence on FLASH sintering of Potassium Sodium Niobate: a relationship with conduction mechanisms," Materials (Basel)., vol. 14, p. 1321, 2021.

[28] R. Serrazina, J. S. Dean, I. M. Reaney, L. Pereira, P. M. Vilarinho, and A. M. O. R. Senos, "Mechanism of densification in low-temperature FLASH sintered lead free Potassium Sodium Niobate (KNN) piezoelectrics," J. Mater. Chem. C, vol. 7, pp. 14334–14341, 2019.

[29] R. Serrazina, A. Tkach, L. Pereira, A. M. O. R. Senos, and P. M. Vilarinho, "FLASH sintered potassium sodium niobate: high performance piezoelectrics at low thermal budget processing," *SUBMITTED*, 2021.

[30] M. M. Gomes et al., "Revisiting the phase sequence and properties of K0.5Na0.5NbO3 ceramics sintered by different processes," Ceram. Int., vol. 45, no. 6, pp. 8308–8314, 2021.

[31] G. Liu, D. Liu, J. Liu, Y. Gao, and Y. Wang, "Asymmetric temperature distribution during steady stage of flash sintering dense zirconia," J. Eur. Ceram. Soc., vol. 38, pp. 2893–2896, 2018.

[32] Y. Li, R. Torchio, S. Falco, P. Alotto, Z. Huang, and R. I. Todd, "Promoting core/surface homogeneity during flash sintering of 3YSZ ceramic by

current path management : experimental and modelling studies," J. Eur. Ceram. Soc., vol. 41, pp. 6649–6659, 2021.

[33] N. Terakado, R. Sasaki, Y. Takahashi, T. Fujiwara, S. Orihara, and Y. Orihara, "A novel method for stress evaluation in chemically strengthened glass based on micro-Raman spectroscopy," Commun. Phys., vol. 3, no. 1, p. 37, Dec. 2020.

[34] M. E. Fitzpatrick, A. T. Fry, P. Holdway, F. A. Kandil, J. Shackleton, and L. Suominen, "Determination of Residual Stresses by X-ray Diffraction - Issue 2," in Measurement Good Practice Guide, no. 52, Crown, Ed. Teddington, Middlesex, United Kingdom: NPL - National Physical Laboratory, 2005.

[35] B. D. Cullity, Elements of X-ray diffraction, Second. 1978.

[36] B. Malič et al., "Sintering of lead-free piezoelectric sodium potassium niobate ceramics," Materials (Basel)., vol. 8, no. 12, pp. 8116–8146, 2015.

[37] S. Priya and S. Nahm, "Development of KNN-Based Piezoelectric Materials," in Lead-Free Piezoelectrics, 1st ed., S. Priya and S. Nahm, Eds. Springer, 2012.

[38] A. Tkach, A. Santos, S. Zlotnik, R. Serrazina, and O. Okhay, "Strain-Mediated Substrate Effect on the Dielectric and Ferroelectric Response of Potassium Sodium Niobate Thin Films," Coatings, vol. 8, p. 449, 2018.

[39] K. I. Kakimoto, K. Akao, Y. Guo, and H. Ohsato, "Raman scattering study of piezoelectric (Na0.5K0.5)NbO3-LiNbO3 ceramics," Japanese J. Appl. Physics, Part 1 Regul. Pap. Short Notes Rev. Pap., vol. 44, no. 9 B, pp. 7064–7067, 2005.

[40] R. M. Badger, "A Relation Between Internuclear Distances and Bond Force Constants," J. Chem. Phys., vol. 2, no. 3, pp. 128–131, Mar. 1934.

[41] R. M. Badger, "The Relation Between the Internuclear Distances and Force Constants of Molecules and Its Application to Polyatomic Molecules," J. Chem. Phys., vol. 3, no. 11, pp. 710–714, Nov. 1935.

[42] S. Kojima, J. Zushi, Y. Noguchi, and M. Miyayama, "Successive phase transition of lead-free ferroelectric sodium potassium niobate crystals studied by Raman scattering," Ferroelectrics, vol. 532, no. 1, pp. 183–189, 2018.

[43] X. Zhao, J. J. Wang, and L. Q. Chen, "A thermodynamic study of phase transitions and electrocaloric properties of K0.5Na0.5NbO3 single

crystals," Appl. Phys. Lett., vol. 116, no. 9, pp. 0–5, 2020.

[44] E. Buixaderas et al., "Lattice dynamics and phase transitions in KNbO3 and K0.5Na0.5NbO3 ceramics," IEEE Trans. Ultrason. Ferroelectr. Freq. Control, vol. 56, no. 9, pp. 1843–1849, 2009.

[45] C. C. Aydiner and E. Üstündag, "Residual stresses in a bulk metallic glass cylinder induced by thermal tempering," Mech. Mater., vol. 37, pp. 201–212, 2005.

[46] J. H. Nielsen, J. F. Olesen, and H. Stang, "Characterization of the Residual Stress State in Commercially Fully Toughened Glass," J. Mater. Civ. Eng., vol. 22, no. 2, pp. 179–185, 2010.

[47] R. Serrazina, A. Tkach, L. Pereira, A. M. O. R. Senos, P. M. Vilarinho, FLASH sintered potassium sodium niobate: high performance piezoelectrics at low thermal budget processing, submitted, 2022.